Lawrence Berkeley National Laboratory

Title

Liquid-free covalent reinforcement of carbon nanotube dry-spun yarns and free-standing sheets

Permalink

Authors

Lepró, Xavier
Aracne-Ruddle, Chantel
Malone, Daniel
et al.

Publication Date

DOI

Copyright Information

Peer reviewed

Liquid-free covalent reinforcement of carbon nanotube dry-spun yarns and free-standing sheets

Xavier Lepró[*,1], Chantel Aracne-Ruddle [1], Daniel Malone [1], Haley Hamza [1], Eric Schaible [2], Steven F. Buchsbaum [1], Alicia Calonico-Soto [1], John Bigelow [1], Eric Meshot [1], Salmaan Baxamusa [1], Michael Stadermann [1]

[1]Physical and Life Sciences Directorate, Lawrence Livermore National Laboratory,

P.O. Box 808, Livermore, CA 94550, USA.

[2] Advanced Light Source, Lawrence Berkeley National Laboratory,

1 Cyclotron Road, Berkeley, CA 94720, USA.

*Corresponding author e-mail: xnlepro@llnl.gov

ABSTRACT: Carbon nanotubes (CNTs) possess exceptional mechanical properties, surpassing stiffness and strength metrics of common materials such as steel alloys by 100× at the nanoscale. However, when myriads of individual CNTs are bundled together into macroscopic ensembles like fibers or sheets, the result is a 100-fold drop in strength compared to its individual components. Here we present a general strategy aimed to close this gap in property scaling. By using vapor-phase polymerization of a crosslinkable polymer, we reinforced the weak interlinkages among individual CNTs within both yarns and sheets to promote a better transference of mechanical load across the structure. After the treatment, dry-spun, low-density 2.3 μm thin yarns increased their elastic moduli by at least 300%, and free-standing CNT sheets exhibited a 10× boost. In-situ synchrotron small-angle X-ray scattering revealed that polymer-reinforced yarns undergo limited CNT bundle rearrangement when subjected to tensile loads compared to pristine yarns. This evidence supports the hypothesis that the polymer hinders CNTs slippage, the root cause of the poor scaling of mechanical properties in these materials. While we demonstrated this reinforcement method for CNT structures, it is not specific to CNTs and could be used in a wide variety of other hierarchical nanostructured ensembles.

1. Introduction

Decades-long attempts to scale the exceptional properties of nanomaterial building blocks to macroscale ensembles have fallen short. In particular, carbon nanotubes (CNTs) are regarded as the strongest nanomaterial due to their covalent carbon-carbon bonds, hexagonal lattice, and cylindrical form factor. Their exceptional mechanical properties (Young's moduli and tensile strengths 100× greater than steel alloys on a per unit weight basis) [1], combined with other attractive electrical and thermal characteristics, have spurred substantial research efforts to construct macroscale assemblies. However, assemblies composed by continuous CNTs are hard to come by and, until recent advances in synthesis resulting in direct growth of CNT assemblies ∼14 cm long [2], we were limited by bundles not larger than a couple of centimeters [3]. Despite great advances in the improvement of CNT yarn performance during the last 20 years, the developed strategies still are using up to merely ∼10% of the mechanical properties of the individual nanoscale components (Young's modulus of ~1 TPa and strength up to 100 GPa). [4] Material-property scaling limitations are evident in spun-CNT yarns that exhibit tensile strengths that can range between 500 MPa [5, 6] and 1.3 GPa [7] by purely tuning the spinning conditions, which is still about 2 orders of magnitude lower than the typical strength of an individual nanotube. Improving this scaling could unlock a new generation of products based on ultra-strong, flexible, conductive fibers for aerospace, defense, communications, wearables, and biomedical industries.

Dry-spinning CNT yarns [5] is a promising route toward macroscale fabrication because it capitalizes on inherent directed-assembly characteristics enabled by vertically aligned CNT arrays ("forests"), whereby internal bundling promotes the formation of continuous sheets and threads upon pulling. Billions of nanotubes coherently align along the pull direction and form a

free-standing web of mechanically interconnected nanotubes with an ultra-low volumetric density of ∼1.8 μg/cm^2. Subsequent twisting transforms drawn sheets into flexible, micrometric-thin yarns with a twisted morphology resembling those of wool and cotton threads used in the textile industry. Thus, meter-long yarns may be composed of a myriad of relatively short individual CNTs that are coupled along their length through non-covalent interactions and van der Waal forces, which define the yarns' ultimate strength. Therefore, yarn failure is then governed by weak forces that allow nanotube slippage [8] rather than the strong covalent carbon-carbon bonds in individual CNTs.

In order to overcome this challenge in performance scaling of CNT ensembles, it is critical to develop strategies for introducing covalent linkages among neighboring nanotubes and effectively distribute load transfer across the strong CNT lattice. The sidewalls of CNTs are known for being chemically inert and not trivial to chemically modify absent harsh chemical conditions [9] like strong hot acids, [10, 11] oxidative methods [12] and plasma, [13] which are detrimental to their structure and mechanical properties. Without such modifications, polymer reinforcement improves the mechanical performance of the yarns [14] by modifying their internal interfacial shear, but the ultimate strength will fall short of the ideal limit without a defined covalent bond between polymer and nanotube [4, 15, 16]. Approaches using agents requiring milder reactive conditions to covalently bond with the CNT sidewall [7, 17-21] have shown to considerably enhance the yarn's mechanical properties (increased strength by ∼50-90% and Young's modulus by ∼3x) because of improved load transfer between the nanotubes and polymeric crosslinker. Typical polymer composite preparation, however, is based on wet methods where CNT arrays or other directed-assembled structures are either immersed or dispersed on molten polymers, their solutions, or precursors. [4, 22, 23] Strategies aimed to

achieve CNT interbundle bridging without requiring prior nanotube chemical functionalization, while successful in increasing yarn strength and elastic modulus (by ~60% and 2.8x respectively), rely on relatively highly energetic methods, such as electron irradiation (> 80 keV) [24] and Joule heating via incandescent tension annealing in vacuum (~2000°C) [25].

Wet-reinforcing methods are problematic for low-density structures that may collapse due to surface tension of imbibing or evaporating liquids. Lack of control of both the amount and location of liquid applied to already-formed CNT structures may also result in excess material that does not actively enhance the mechanics and thus detracts from the overall "per weight" performance metrics. Recent work demonstrated conformal polymeric coatings of nanoscale features [26-28] by initiated chemical vapor deposition (iCVD) on intricate, low-density CNT structures. Unlike other CVD infiltration methods, [29, 30] iCVD does not require the relatively high temperatures (650 - 750°C) of thermal CVD and is carried out close to room temperature instead (Figure S1). The promise of vapor-phase iCVD polymer synthesis for reinforcing nanostructures is rooted in its *in-situ*, free-radical process that occurs during controlled monomer absorption on a surface [31] in a liquid-free environment, which minimizes the risk of structural collapse. [32, 33]

iCVD polymerization represents the intersection of all-dry and scalable technology with the chemistry of functional organic materials that can be applied to nearly any substrate at low surface temperatures. In a single step, vapor-phase monomers undergo selective reactions to produce high-purity, conformal, and durable polymeric layers. [34] Using the vapor-phase is especially advantageous for treating highly porous, hierarchical materials since monomers are more efficiently transported through the confines of the structure than by a liquid-phase due to its

lower viscosity and density. By eliminating the need to dissolve macromolecules, iCVD allows the synthesis of insoluble polymers and highly crosslinked [35] organic networks and the copolymerization of pairs of monomers lacking a common solvent with the additional advantage of avoiding unwanted side reactions that may occur in solution. [34]

Here, we devise a strategy based on iCVD of a thermally self-crosslinking polymer to reinforce CNT yarns and enhance their elastic moduli by 300%, the same order than other methods requiring nanotube functionalization. Yarns spun under low tension to diameters as thin as 2.3 μm increased their Young's modulus from 20 to 80 GPa. This value is in pair with other reported for twist-spun CNT yarns, considering their diameter and specific mass, representing improvements attributed to a homogeneous iCVD coating and local cross-linking bonds that resist slippage between CNTs. We apply classical transport-reaction theory to highlight that diffusion rates of the monomer in this study dominate the polymerization kinetics, which enables the highly uniform coating observed in our CNT structures by SEM. *In situ* tensile loading during synchrotron small-angle X-ray scattering (SAXS) reveals quantitative evidence that the anisotropic CNT morphology in iCVD-coated yarns is more stable at higher internal stresses compared to pristine CNT yarns. In addition to 1D yarns, we also explore covalent linking of freestanding assemblies comprising orthogonally stacked 2D sheets while retaining their unique crosshatch structure. The superior 2D elastic modulus of these CNT sheets surpasses benchmark freestanding polymeric films and demonstrates the versatility of this novel vapor-phase technique for building macroscale assemblies from nanoscale subunits. Our analysis of this liquid-free, covalent reinforcement strategy and accompanying mechanistic understanding from structural characterization addresses key questions about performance scaling of emergent nanomaterials. Insights derived here are expected to advance fabrication of low-density, high-

performance nanostructured materials by providing an effective route to engender the elite nanoscale properties into macroscale materials.

2. Experimental

2.1. CNT synthesis and fabrication of CNT assemblies

Spinnable carbon nanotube forests were grown on silicon substrates at near-atmospheric pressure CVD at 700°C using acetylene (C_2H_2) as carbon precursor, Ar/H_2 (12 vol.%) atmosphere and an electron beam-evaporated iron thin-film as catalyst. Details for the CNT synthesis are described elsewhere [36]. Typical CNTs synthesized at these conditions are multiwalled (~8 walls), ~250 μm long, and ~11 nm in outer diameter.

CNT yarns were dry-spun by first pulling a short ribbon of controlled width ($\leq$ 1 mm) from the forest and fixing its end to the rotating axis of a motor. Subsequently, both the forest and motor were displaced in opposite directions during twist insertion to form a yarn with the desired number of turns per length (twist density, m^{-1}) and total length of about 50 cm. Typical yarns used in this study had twist densities between 40,000 and 50,000 turns/m and diameters below ~10 μm. Sections between 1-2 cm of each yarn were cut and transferred onto paper holder frames for their safe manipulation prior to and during mechanical testing. On each holder, the yarn lies free-standing along a central aperture that is ~1 cm long with its extremes fixed to the paper holder edges using an UV-cured epoxy resin. Each specimen diameter is measured at several positions along its length by SEM (Phenom Pro X) prior to mechanical testing. CNT sheet areal density was obtained by measuring the absorbance of polarized light at λ = 550 nm (α = 0.1029 cm^2/μg) passing through a sheet stack oriented parallel and perpendicular to the incident light. Values of areal density were computed by the Lambert-Beer law, A = $\alpha \cdot$C. α is the correlation (r^2 = 0.992) of absorbance A with the mass of sheet stacks of overlaying sheets (n_i= 2, 4, 6, 8) about ~7 cm^2 in area weighted on a microbalance. Yarn's masses were too small for microbalance measurements, so we relied on X-ray analysis as described below and in the Supporting Information.

Free-standing CNT sheets arrays were prepared by direct drawing from the forest edge without twisting and then transferring to rigid open frames (e.g. copper gasket) with alternating orthogonal overlays to create a crosshatch structure. To prevent sheet slippage from the frame during the mechanical testing, its edges contacting the frame were wet-densified with a volatile solvent (typically isopropanol) to ensure an intimate contact between both materials.

2.2. iCVD polymer synthesis

CNT assemblies were coated with poly-glycidyl methacrylate (PGMA) by iCVD (GVD Co. *iLab* coating system) at 200 mtorr using glycidyl methacrylate (GMA, Sigma-Aldrich, 97%) as monomer, *tert*-butyl peroxide (TBPO, Sigma-Aldrich, 98%) as initiator, and a hot filament held at approximately 155°C. During deposition, the TBPO flowrate was maintained at 0.6 sccm while the GMA vapor was allowed to flow unmetered through a 5 mm diameter orifice from a container of liquid GMA heated to 30°C. iCVD is an adsorption-based process driven by the substrate which is maintained close to room temperature (25°C) during the polymerization. CNT yarns supported on paper frames were placed directly on the temperature-controlled surface to maintain the deposition temperature. Still, the free-standing length of the CNT yarns was ~150 μm above the T-controlled surface during deposition due to the thickness of the paper holders used. Free-standing CNT sheets supported on the copper gaskets were raised 2.2 mm above the surface of the chamber, but given the larger thermal conductivity of Cu than paper, we expect the temperature of CNT sheets to be close to that of the stainless steel (SS) chamber surface given the similarity between their thermal conductivities ($\kappa_{CNT\ sheet,\ \parallel} = 50$ W·m^{-1}·K^{-1} [37] and $\kappa_{SS\ 25°C} = 15$ W·m^{-1}·K^{-1} [38]). Polymer thickness was monitored *in situ* during deposition by interferometry of a laser beam (He-Ne, $\lambda = 632.8$ nm) incident on the surface of a silicon wafer

witness as described elsewhere [39]. The PGMA deposition rate on the reference substrate placed directly on top of the chamber substrate surface was 4 nm/min. While the ratio between partial pressure (P_{GMA}) and saturation pressure (P_{sat}) of GMA, P_{GMA}/P_{sat}, is 0.74 at the surface of the deposition chamber, its value is expected to be lower at the suspended CNTs since their local temperature will be higher. An increase of 10°C on the substrate temperature decreases P/P_{sat} to 0.34, a value shown to be within the threshold to attain conformal (step coverage > 0.5) deposition by iCVD on large aspect-ratio porous structures [26, 40]. Detailed experiments of the polymer deposition in the vicinity of CNTs within the yarn are out of the scope of this report and will be part of future studies.

2.3. Polymer self-crosslinking procedure

PGMA-coated CNT materials were thermally treated in a vacuum furnace at 150°C for 30 min under a continuous nitrogen bleed ($P_T \sim 40$ torr) to induce self-crosslinking in the PGMA through an epoxy ring-opening reaction [41]. Free-standing CNT sheet arrays were exposed to an additional intermediate step to ensure separate stacked sheets were in proximity to each other during the thermal cross-linking procedure. A mist of a vaporized isopropanol or acetone was generated by an ultrasonic humidifier (USB 5 V) to partially collapse adjacent sheets in the thickness (z) direction after the mist evaporated.

2.4. Mechanical testing

PGMA-reinforced and untreated CNT yarns were tested in a custom-built elongation/indentation testing machine composed of an *xy*-adjustable stage (Newport M-460A) attached to vertical linear translator (Newport MFA-CC with a minimal displacement motion of

0.1 µm and resolution of 0.018 µm). This ensemble moves normal to a high-precision balance (Mettler-Toledo WM124-122 with a 121 g load cell and 0.1 mg resolution) that doubles as substrate holder and records the force exerted during the mechanical tests. Further details of the setup of our test system are described elsewhere [42, 43]. Both displacement and force are recorded as function of time to generate stress-strain curves of materials under displacement control. During a typical test, one of the paper frame edges containing the CNT yarns is fixed to the end of the linear vertical actuator (that moves in +z) while the opposite end is attached to the bottom balance that remains static during the test, so that the CNT yarn is parallel to the actuator movement (See Results and Discussion). Both ends of the paper frame are fixed to the testing device using an UV-curable epoxy resin. Before starting the elongation test, the paper holder is cut transversally to expose the CNT yarn to the full load during the tensile tests. Force was converted to engineering stress (σ) using the average diameter value measured on individual, unstrained yarns through SEM. The typical yarn length used in these tests was close to 1 cm which is much larger than the typical length of individual nanotubes (~250 µm).

Cyclic tensile tests were done by elongating the CNT yarn in cumulative, reversible steps of 100 µm that each correspond to 1% strain in the yarn in sequential, stepwise fashion at a constant elongation rate of 100 µm/min. In a typical experiment, during the first cycle, a yarn was stretched 100 µm and then returned to its original unstrained state, $\varepsilon = 0\%$. A second cycle encompassing a reversible yarn stretching step of 200 µm then follows, then a third cycle of 300 µm in amplitude and so on until yarn failure.

Indentation tests on free-standing CNT sheets were performed by replacing the edge of the vertical actuator with a 2 mm diameter sapphire sphere to act as a spherical punch as shown in Figure S5. Indentation samples were prepared by transferring the freestanding films onto

bulkhead rings that are 4.5 mm in inner diameter and exhibit a 0.5 mm thick rim. [43] Thick polyimide (PI) films (LUXFilm, Luxel corporation) 40 nm in thickness were tested on the same conditions and used as reference materials for comparing the behavior of the CNT sheets free-standing sheets. A stiffer, carbon-reinforced version of the polyimide films ("PI+C") was prepared by evaporating an ∼8 nm carbon layer on the PI films before they were mounted on the bulkhead rings used for mechanical testing.

2.5. Structural characterization of CNT yarns

We performed nondestructive synchrotron experiments at the Advanced Light Source (ALS) to evaluate the density of CNT yarns *ex situ* by mass attenuation (Beamline 5.3.2.2, 11.0.1.2) along with their nanoscale morphological responses to tensile loading during *in situ* small-angle X-ray scattering (Beamline 7.3.3) [44, 45]. Further details for these measurements are described in the Supporting Information file.

Cross-sections of CNT yarns were obtained by cutting ∼ 4 μm thin yarns fixed ∼ 1 mm above a Si substrate orthogonally to their length using a focused Ga ion beam (FIB FEI NanoLab600i DualBeam) at an accelerating voltage of 30 kV and beam current of 6.5 nA. After the initial cut, the yarns' cross-sections were ion-polished through sequentially decreasing currents down to 48 pA. Then, the samples were transferred to a high-resolution SEM (Apreo S, ThermoFisher Scientific operated at 5 kV) with their cross-sections oriented normal to the electron beam detector to obtain tilt-free images of the yarn's internal morphology.

3. Results and Discussion

3.1. Polymer coating on CNT assemblies

During iCVD deposition (Figure 1A), the peroxide initiator decomposes around the vicinity of the heated filaments, generating reactive radicals that initiate the polymerization of GMA (see Experimental) directly on the surface of the CNTs [32] (Figure 1B). PGMA was selected as a reinforcement agent because its epoxy functional groups undergo self-crosslinking through a thermally-driven, ring-opening reaction (at $\geq 120°C$) [41], providing tunability in the chemomechanical properties with a facile post-treatment heating step (Figure 1C).

CNT assemblies like dry-spun yarns and sheets have intrinsic internal porosity [36, 46] formed by voids between bundles, which create paths for vapor-phase reagents to diffuse. However, the monomer diffusion transport process competes with monomer depletion governed by the kinetics of the polymerization reaction at the CNT surface, which is captured by the Thiele modulus (ϕ_n). This parameter is a dimensionless number that relates the nth-order surface reaction rate to the diffusion rate of the reagent within a porous structure. At the low conversion rates for GMA observed in this study ($\leq 6\%$), the polymerization reaction follows a zeroth-order kinetics [47], so for radial diffusion towards the center of a porous cylindrical structure (i.e., a CNT yarn or bundle), ϕ_n is defined as:

$$\phi_0^2 = \frac{k_0 \cdot r^2 \cdot S_a \cdot \rho_c}{D_e \cdot C_{A_s}} \tag{1}$$

where k_0 is the reaction kinetic constant, r is the radius of the porous substrate, S_a is the specific surface area of the substrate, ρ_c the porous substrate density, D_e the effective diffusivity of the monomer and C_{A_s} the concentration of the monomer at the exterior surface of the porous substrate. When $\phi_0 > 1$, the transport is a diffusion-controlled process, while $\phi_0 < 1$ suggests a process that is limited by the surface reaction rate. For the case of yarns, the effective diffusivity of GMA was computed by the Knudsen expression,

$$D_e = \frac{\lambda}{3} \sqrt{\frac{8\,RT}{\pi\,M_A}} \tag{2}$$

where λ is the mean-free path of the monomer within the yarn, a characteristic length here considered to be the average CNT interbundle spacing $\lambda \sim 100$ nm; M_A is the molecular mass of GMA (142.15 g/mol), T is the absolute temperature (295 K) and R is the universal gas constant. Substituting these values into equation (2) yields $D_e = 7 \times 10^{-2}$ cm^2/s.

Formally, the CNT interbundle spacing within dry-spun yarns varies across their cross-section. It becomes shorter at the yarn's core with respect to the outskirt regions as consequence of the helically driven forces that arise from twisting a mostly 2D free-standing sheet used as starting material. The radial difference in porosity forms a core-sheath structure that becomes more pronounced with large twist densities. While the above computed D_e is an average value attempting to approximate the overall structure of the yarn, the value at its core could be estimated by using a smaller interbundle spacing, of the order of a single CNT diameter ($\lambda \sim$ 10 nm), which yields a D_e one order of magnitude smaller, 7×10^{-3} cm^2/s.

We extracted the kinetic constant for the iCVD polymerization reaction ($k_0 = 2.7 \times 10^{-11}$ mol·cm^{-2}·s^{-1}) from experimentally determined growth rates we measured for PGMA on nonporous substrates ($\sim$4 nm/min). We estimated the specific surface area $S_a = 1.2 \times 10^4$ cm^2/g by considering a CNT yarn $\sim$6 μm in diameter, comprised of 11 nm MWCNTs at a mass density $\rho_{yarn} = 0.56$ g/cm^3, which we measured by mass attenuation (Figure S2).

All these values substituted in equation (1) provide a Thiele modulus that ranges from $\phi_0 = 6.2 \times 10^{-4}$ at the yarn's periphery to 1.9×10^{-3} at its core, since both are less than unity it implies mass transport within the CNT assemblies is reaction-limited. The monomer is expected to diffuse homogeneously to create a uniform, conformal polymer coating throughout the thicknesses of CNT assemblies as observed by in their cross-sections by SEM (Figure 3). Thus,

the reinforced CNT assemblies are uniformly interconnected by polymer chain linkages, which leads to significant enhancements in their mechanical properties as discussed in the next section. As ϕ_0 is several orders of magnitude smaller than 1, the reaction-limited regime suggested above should be valid down to the thinnest $\sim 2.3\ \mu m$ yarns studied in the present report.

3.2. CNT yarns

During twisting, CNT bundles are compressed by helically driven forces that consequently reduce void spaces, yet porosity remains due to inherent limits of packing polydisperse, tortuous nanostructures. We nondestructively quantify the CNT yarn porosity by mass attenuation prior to polymer infiltration using a soft X-ray synchrotron beamline. The average density of uncoated CNT yarns with diameters ranging from 5.5 to 6.5 μm was 0.56 g/cm^3 $\pm$ 5.1$\times$10^{-2} g/cm^3 (see Figure S2) yielding a mean volumetric porosity of 0.73 based on the expression $\varphi = 1 - \frac{\rho_{yarn}}{\rho_{CNT}}$, where ρ_{CNT} is the average density of the carbon in the CNT walls (2.1 g/cm^3 [48]). For comparison, the maximum theoretical density of parallel, close-packed CNTs that are 10 nm in diameter is 1.6 g/cm^3 ($\varphi = 0.24$) [49]. We tuned the iCVD coating to fill a fraction of this porosity and introduce cross-linking between neighboring CNTs without adding excessive polymer mass. For this study the coating was equivalent to 200 nm as measured on a witness silicon wafer, which is larger than the average spacing between CNTs and corresponds to only about 10% of the total mass of a coated yarn. While understanding the precise filling mechanism is part of ongoing research, we expect the local surface area being greater than the flat silicon leads to interconnected CNTs and bundles with some void space remaining as we observed in the yarns' cross-sections (Figure 3). Furthermore, the lack of statistical difference in yarn diameter before and after coating (Figure 2) signifies a uniform coating throughout the high surface-area

yarn substrate absent excessive accumulation on yarns' outer surfaces. Imaging of the cross-sections of yarns prior and after polymer coating by iCVD (Figure 3) corroborates a homogeneous radial polymer infiltration thorough the yarn core, despite the local differences in porosity of the original yarn (Figure 3A and C). While voids are significantly reduced by ∼80% on the coated yarns (Figure 3B and D), they still represent about 4% of the yarn's cross-section area.

To evaluate the influence of chemical cross-links on the mechanical performance of CNT assemblies, we analyzed the pristine CNT yarns compared to those that were iCVD coated and thermally treated. The Young's modulus of crosslinked-polymer reinforced yarns increased by more than 300% with respect to uncoated, pristine yarns (Figure 4A). Indeed, PGMA-coated yarns without the thermal cross-linking step exhibit some benefit from the additional interstitial material (80% stiffer than pristine yarns, Figure S4A). Some yarn densification is expected after thermal treatment due to minimal reflow of the polymer. While densifying yarns (e.g., with a solvent) is known to increase van der Waals interactions and thus the Young's modulus (e.g., ~16% increase by using acetone), [50] this effect cannot solely explain the substantial gains observed from cross-linking iCVD coated yarns. This underlines that the creation of strong self-crosslinking units within the polymer coating is responsible for the majority of the modulus enhancement. Despite the significant improvement, we note a corresponding decrease in the ultimate strain from 12% to 4% after coating, which we examine in greater detail later along with ultimate strength and yarn diameter effects. It is important to note that wet densification leaves the ultimate strain of yarns unchanged [50] and thus strain reduction is a consequence of the crosslinks rather than a result of increasing internanotube frictional forces by enhancing physical contact.

To further investigate the viscoelastic and plastic behaviors introduced by cross-linking, we performed experiments (see Experimental) and extracted the effective Young's modulus (E_{eff}) from the slope at the beginning of each loading and unloading curve. Taken together, the cycles for both types of yarns represent well-defined hysteresis loops typical of viscoelastic and viscoplastic materials (Figure 4B). Within a single hysteresis loop, the modulus of as-spun yarns during unloading is larger than during loading (Figure 4C) which, together with the unrecoverable strain observed on yarns upon finishing the unloading, are indicative of structural reorganization that we attribute to CNT slippage (drafting). The same behavior is observed for treated yarns, yet the difference between unloading and loading E_{eff} at the highest strains before failure is reduced from 380% to 69% due to the presence of the polymer reinforcement. On loading, treated yarns exhibit a E_{eff} that is 320% larger than the one of pristine yarns (19.5 ± 0.8 vs 6.1 ± 0.5 GPa), and is comparable in value to the moduli measured during the unloading of pristine yarns that have been cyclically strained close to 5%. The amount of induced unrecoverable strain in reinforced yarns is also dramatically reduced to 0.6%, compared to $\sim 6.5\%$ in pristine yarns. Furthermore, the amount of unrecoverable deformation is related with the length that CNTs can migrate through displacement and axial realignment along the internal structure of the yarn before the integrity is compromised. For instance, in a typical yarn test specimen 10 mm long, the reorganization length prior to failure ($\varepsilon = 6.5\%$) corresponds to a migration distance of 650 µm, which is about 2.5 times the length of individual CNTs. We observe that pristine CNT yarns deform plastically over a full strain range of about 12%, reversibly losing 66% strain energy per cycle (above 3% strain). Even though energy losses are observed after each cycle on cross-linked yarns, they are, on average, 38% smaller than in untreated yarns and only reach a maximum at 48% at 3% strains before yarn failure

(ε_{break} = 3.9%). This indicates the majority of CNTs are effectively anchored with respect to each other, which hinders their tendency to translate in response to increasing strains and leads to invariant measurements of Young's modulus across reloading cycles. Next, we explore a more granular view of how enhancements from cross-linking manifest differently depending on the yarn diameter.

As yarn diameter decreases, the Young's modulus (E) of crosslinked-polymer reinforced yarns increased nonlinearly, reaching up to 80 GPa for diameters close to 2.3 μm (Figures 3D and S4). The modulus follows a reciprocal power law with yarn diameter with a fitted power close to that expected for area scaling of the cross section for a given twist density, $E \sim d^{-2}$ ($E \propto d^{-1.92}$, r^2=0.9948, N=17). We found these fitted values hold within a ~10% ($E \propto d^{-1.71}$, r^2=0.8842) in statistical analysis on larger sets of yarns exhibiting variations in twist density within 12% (Figure S4B). Normalizing mechanical properties of the yarns by linear mass density enables performance comparison across diameters, which is conventional in textiles and is expressed in tex units (1 tex = g/km). Linear densities for yarns in this study were determined by combining volumetric mass density values from X-ray characterization and yarn diameters measured from SEM. By taking into account the increase in yarn density after adding the polymer, we note that the level of improvement in normalized Young's modulus Ê with cross-linking is independent of yarn's diameter (Figure S4C): 2.6x for 5.2 μm (8 to 23 N/tex) and 4.0 μm (15 to 40 N/tex), 2.7x for 3.1 μm (22 to 58 N/tex) and 2.4x for the thinnest, 2.3 μm yarns (34 to 83 N/tex), which is consistent with the estimated ϕ_0 << 1 for the polymer deposition reaction. Similarly, the yarn's median specific strength at failure diminishes by ∼30% after polymer crosslinking independently of diameter, at least for values below ≤ 5.5 μm (Figure S4D). In larger yarns, the specific strength decreases from 0.63 to 0.42 N/tex prior to and after crosslinking, while in the thinner

yarns (~2.3 μm) the change is from 1.1 to 0.80 N/tex. Similar loses of up to 40% in the specific strength of 1-ply CNT yarns reported after liquid-polymer impregnation cannot be fully explained by variations on the polymer content in the final composites or by other yarn post-fabrication processing. [51] Composite systems based on CNT yarns (> 40 vol. %) do not typically follow the rule of mixtures of two individual components and their mechanical properties are mostly determined by those of the original yarns rather than compositional changes of a reinforcing polymeric matrix. This is derived from the limited free volume available within the CNT yarn bundles which severely constrains the local mobility of the polymeric macromolecules and limits the deformation mechanisms they can incur under an external load or temperature change, leading to a behavior substantially different from conventional composites. [52]

Electron microscopy of the polymer-reinforced CNT yarns after tensile fracture (Figure 2D-F) suggest that the nanotubes are well-wetted by the crosslinked polymer at the bundle level (Figure 2F) and do not appear to undergo polymer unsheathing during the tensile loading that resulted in yarn failure. The fracture of the polymer-reinforced yarn (Figure 2E) is consistent with the brittle behavior observed in the tensile tests, without showing the shear-fracture mechanism typically observed on dry-spun yarns due load-induced CNT bundle migration (Figure 2D). Decrease in the yarn specific strength upon reinforcement with polymer crosslinking thus may be result of the local accumulation of stresses in an area of the yarn since they cannot be relaxed through CNT bundle migration because of polymer hindrance. The CNT movement is restricted, less plastic deformation occurs, and larger tensile loads are required as threshold to start it (Figure 6C). Within a bundle, the relaxation processes, which depend on the polymer matrix cross-linking density, are suppressed by the densely packed CNTs given the limited free volume

available for local polymer chain movement (in the ~10 nm range), thus decreasing its ductility in the composite. So, instead of the yarn failing by CNT slipping and drafting, it does by transferring the load locally to the interlocking epoxy polymer, which ultimately fails while its load limit is reached since it cannot deform to redistribute or dissipate the stress. In epoxy networks, the macromolecular chain flexibility has a greater importance for the defect nucleation than the density of cross-linking bonds. Therefore, increasing the polymer chain stiffness or reducing the local mobility of the epoxy macromolecules can increase the rate of the defect initiation and propagation, thus making the material more brittle. [52] Accumulation of these stress-induced defects within the crosslinked-polymer phase acting as reinforcement ultimately leads to the yarn's catastrophic failure.

Hindered interbundle migration via polymer linkage enables yarns to support larger loads at smaller plastic deformations, which can be advantageous for precise alignment of micrometric structural components. A single reinforced ~6 μm CNT yarn is strong enough to support loads ~600 times their mass while exhibiting a minimal deflection as shown in Figure 5. Despite featuring a mass of only ~17 μg, the reinforced yarn only deflects by tens of micrometers (~30 μm from an initial taut position, $\varepsilon_0 = 0.5\%$) over a length that is 1,000 times its diameter under the 8.2×10^{-5} N load. Such lateral displacement is equivalent to introducing an additional strain of only 0.015%. To put this value in context, a hypothetical 316 stainless steel rope of similar dimensions would strain 10 times more ($\varepsilon \sim 0.1\%$) supporting a load 600x its own weight.

We probed the nanoscale morphology of CNT yarns with complementary *in situ* SAXS experiments to validate our hypothesis that introducing cross-linking indeed restricts the translation of CNTs under loading. We collected 2D SAXS images during quasi-static tensile

loading (Figure 6A) and subsequently integrated the azimuthal intensity at the q position corresponding to the CNT core-shell form factor. Therefore, extracting the full-width at half maximum (FWHM) provided an ordinal measure of the distribution of angular alignment of CNTs within the yarn (Figure 6B), which is expected to narrow under tensile loading as CNTs straighten. We plotted the FWHM with respect to its initial value as a function of the yarn's stress response to the applied strain to represent the relative fractional change in CNT alignment (Figure 6C). Both pristine and cross-linked yarns exhibited straightening of their CNTs under applied tensile stress, yet the morphological evolution in the cross-linked yarn was comparatively less sensitive to stress. Up to ~125 MPa, the CNT alignment within the cross-linked yarn was nearly invariant, and the rate of change thereafter was only 0.2% MPa^{-1} versus 0.5% MPa^{-1} for the uncoated yarn. In contrast to the cross-linked sample, CNTs in the uncoated yarn immediately begin to straighten followed by a slight decrease in the slope in Figure 6C at high tensile stress, which may be symptomatic of the onset of slippage between CNTs. The structural deformation of CNT yarns is generally driven by the progressive, local failure across hierarchical length scales. Larger CNT bundles that are loosely connected begin to migrate first under stress, followed by more tightly packed and strongly bound individual CNTs. In coated yarns, both cleaving of covalent linkers and CNT slipping may occur simultaneously within the yarn but perhaps not at identical local regions. SAXS analysis indicates CNT bundles and individual CNTs in the absence of covalent linkers readily rearrange (i.e., straighten) and slip. These results provide quantitative structural details in support of our claims that iCVD coating engenders cross-linking that effectively resists CNT migration otherwise known to limit the stiffness and strength in pristine yarns.

3.3. CNT free-standing sheet assemblies

The vapor-phase reinforcement strategy not only reinforces adjacent CNTs within a single assembly, but it also covalently links together multiple assemblies toward building hierarchical structures that are mechanically enhanced. As a proof of concept, we stacked multiple anisotropic CNT sheets created by uniaxial drawing from CNT forests (without inserting twist, as usually required for yarn formation). Stacking these sheets orthogonally with respect to each other achieved a meshed crosshatch structure, wherein each ~ 18 μm layer [53] is comprised of sparsely distributed CNTs and bundles at < 2% areal density. To fabricate unified structures, we ensured maximal inter-sheet contact through controlled capillary densification by exposing sheet assemblies to a solvent mist after PGMA coating. This way, the thermal cross-linking processing step finally glues multiple layers together that otherwise were only in weak/infrequent contact with each other. After cross-linking, the CNT composite structures retain a 2D mesh-like structure at different hierarchical levels (Figure 7A) and their mechanical properties suggest the entire stacked ensemble is substantially reinforced compared to pristine stacked sheets either as drawn or mist-densified.

We quantified the mechanical properties of these stacked sheets (meshes), mounted as free-standing circular films, by measuring their force-displacement behavior with a spherical indenter (Figure S5). This process can be described by accounting for contributions of a pre-tension term (linear) and a large-displacement (cubic) as described by Lee et al. [54] in the expression:

$$F = \sigma_0^{2D}(\pi\, a)\left(\frac{\delta}{a}\right) + E^{2D}(q^3 a)\left(\frac{\delta}{a}\right)^3 \tag{3}$$

where F is the applied point force on the center of the circular CNT mesh, σ_0^{2D} is the pretension in the film, a is the diameter of the CNT mesh, δ is the displacement at the central point, and

$$q = (1.049 - 0.15\nu - 0.16\nu^2)^{-1} \tag{4}$$

is a dimensionless constant related to the material's Poisson's ratio (ν). The superscript 2D indicates that the strain energy density is normalized by the area of the sheet rather than by the volume (as normally would be for bulk materials) as the ratio of film diameter to thickness is $\sim10^5$. Equation (3) is valid for indentation depths that are less than ~0.200 mm [43], in which case the radius of the indenter may be ignored [43, 55] and the use of 2D mechanical property descriptors (i.e., E^{2D}, σ^{2D}) instead of bulk ones is justified; however, bulk properties may be recovered by dividing these 2D quantities by film thickness. We consider $\nu = +0.22$ for our CNT meshes as an approximation derived from multiple in-plane modes reported in the literature [56], so the dimensionless constant q for the stacked sheets from Equation (4) is 0.99. For reference, most materials have a positive Poisson's ratio around 0.33, [56] while graphite is 0.165 [57] and our reference material, polyimide, is 0.34 [58].

Figure 7B shows force-displacement curves obtained for indentation depths up to 200 μm from stacked CNT sheets with various treatment conditions compared to 40 nm-thick polyimide films as benchmark materials. Fitting these curves with a cubic function as described by equation (3) yields fitted constants that estimate the film pretension stress and elastic modulus (see table 1). Polymer reference films exhibit similar pre-tension values because they were transferred onto the fixtures for mechanical testing using the same procedure (glued to rim with epoxy resin). The pre-tension in the set of CNT sheets monotonically increases from pristine to densified to cross-linked (0.16, 0.37, 1.02, respectively), which signifies the progressively increasing hinderance of CNT bundle slippage within the sheets.

The most interesting behavior in relation to enhancements in mechanical performance is rooted in the 2D elastic moduli of the different films in Figure 7C. While mist densification increased E^{2D} for the free-standing arrays by 3.7x (from 459 to 1702 Pa·m) due to enhanced physical and

van der Waals interactions, it is still below those observed for the continuous polyimide films. However, as established for the yarn case, densification alone was not sufficient to reproduce the substantial enhanced observed when the CNT sheet was coated and reinforced via PGMA crosslinking. Specifically, reinforcement boosted the E^{2D} of the free-standing CNT structures by 2 orders of magnitude (13 MPa·m). This is an order of magnitude larger than pristine polyimide (2 MPa·m) and twice the value of carbon-reinforced polyimide, even though the density of coated, stacked CNT sheets is less than half of the reinforced polyimide (3.6 μg/cm^2 versus 7.6 μg/cm^2, respectively). Although it is difficult to make direct comparisons with yarns, the magnitude of the CNT sheets property improvements is comparable to those observed for CNT yarns, thus illustrating the utility of our iCVD-based approach for building up polymer-reinforced CNT assemblies.

4. Conclusions

We demonstrate that a vapor-phase method based on iCVD reinforces porous nanostructure assemblies without inducing their structural collapse. By using minute amounts of specially engineered cross-linkable polymers, CNT yarns withstand larger mechanical loads at smaller strains, which we attribute to a restricted CNT bundle mobility. Consequently, the elastic modulus of the yarns increased up to 300% and values of 80 GPa were measured on yarns as thin as 2.3 μm in diameter. Strong interlinkages among the otherwise weakly interconnected CNTs provide more efficient load transfer within the CNT scaffold. After treatment, 2-D CNT free-standing meshes increase their mechanical stability by a factor much larger than a simple enhancement of physical interconnections that partial densification could explain. These strong, free-standing 2D meshes of highly oriented CNTs are not possible to obtain in a direct way by utilizing methods involving liquid phases, and thus our methodology provides a new path to generate micro- and macro-scale structures that could be of interest in the field of mesoporous materials and membranes. The iCVD method presented in this work is not specific to a CNT chemistry and can be extended to reinforce most porous or fragile nanostructure arrays. Since iCVD allows for polymer design, we envision future uses expanding as polymer libraries are designed for increasing or changing specific material (multi-functional) properties in addition to mechanical behavior. Moreover, the deposited polymer can be selected to exhibit specific interactions and/or a chemical affinity with the nanostructured scaffold if so needed.
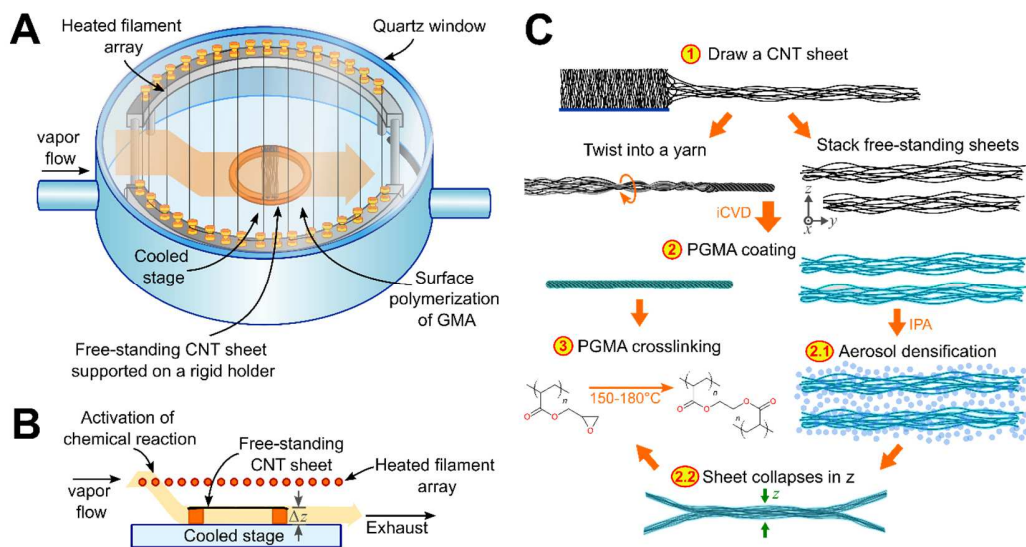
Figure 1. Polymer Reinforcement Procedure for CNT Sheet Assemblies. (**A**) **iCVD reactor and experimental setup.** Schematics of the reactor used for the initiated chemical vapor deposition (iCVD) of the polymer used for structural reinforcement. During iCVD, vapors of monomer and initiator are delivered into a low-pressure chamber equipped with a temperature-controlled stage to regulate monomer adsorption. An array of heated filaments placed above the stage provide the activation energy required for thermolysis of the initiator and activation of the polymerization reaction. (**B**) **Side-view of the reactor chamber**. To avoid surface shadow effects during polymer deposition, free-standing CNT array-structures are mounted across rigid open-holders, which place them a few millimeters (Δz) above the temperature-controlled stage surface. (**C**) **CNT yarn or sheet formation.** CNT yarns are formed by inserting twist into free-standing sheets drawn from CNT forests. On untwisted, free-standing CNT sheets, CNT bundles are sparsely distributed across the thickness (*ie.* z-direction), separated by distances spanning from hundreds of nanometers to few micrometers, as shown in the lateral view drawing (along the z-axis) of two independent free-standing CNT sheets stacked on top of each other (**1**). These free-standing arrays are then exposed to an iCVD process (**2**) to coat them conformationally with

poly-glycidyl methacrylate (PGMA) at the bundle level. (**2.1**) PGMA-coated free-standing CNT sheets are then exposed to a solvent aerosol (IPA, acetone, EtOH, etc.) that collapse them along their thickness and (**2.2**) increases CNT-bundle contact by bringing individual bundles closer to each other. After aerosol densification, PGMA-coated CNT bundles become in intimate contact with each other through their outer polymer layer. (**3**) Crosslinking among polymer surfaces in intimate contact is then induced by exposing the assemblies to a thermal treatment between 150-180°C by half an hour in an oxygen-depleted atmosphere.
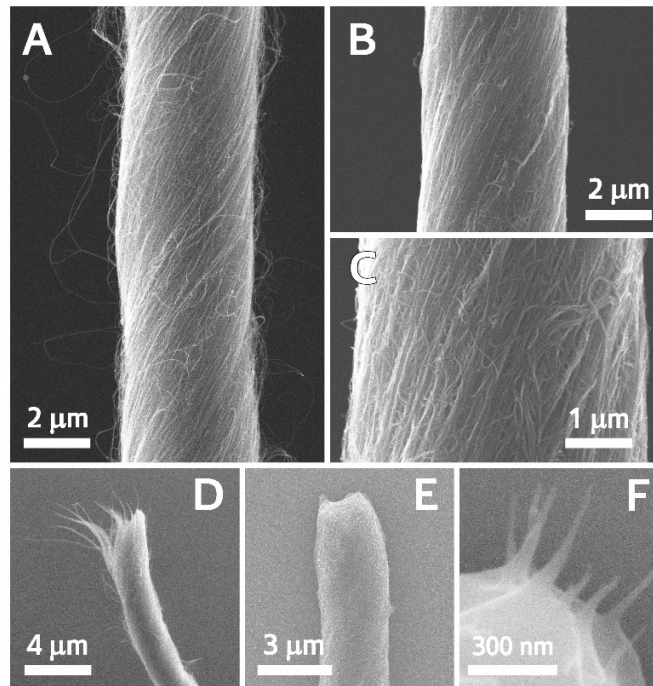
Figure 2. Dry-Spun Carbon Nanotube Yarns (**A**) before and (**B**) after PGMA coating and thermal crosslinking. (**C**) High magnification of (B) shows that after crosslinking, the polymer coats the yarn at the bundle level. Fracture of an (**D**) untreated and (**E-F**) crosslinked-polymer CNT yarn after tensile testing. High magnification (F) shows no signs of CNT-polymer unsheathing at the fracture site.
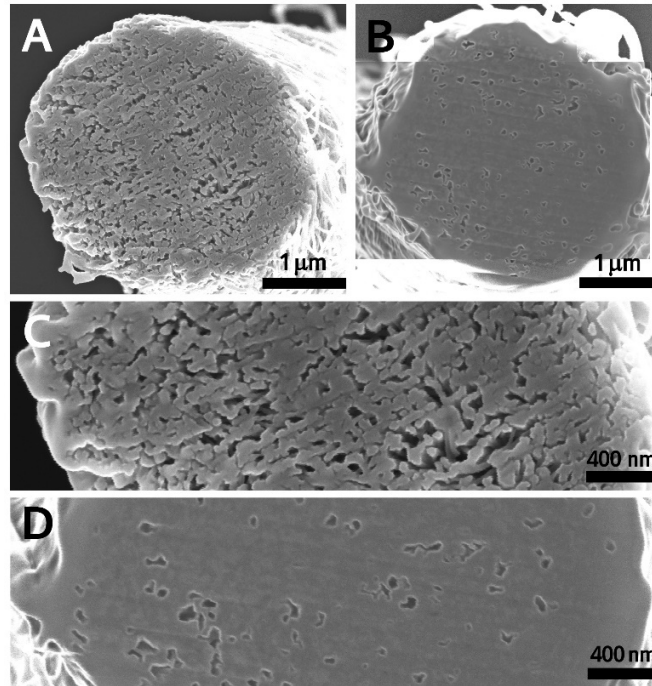
Figure 3. Cross-sections of CNT yarns (**A, C**) before and (**B, D**) after iCVD PGMA coating. High magnification images show the yarn porosity along their diameters. The decrease of porosity in (D) is the result of the incorporation of PGMA through the yarn's internal structure. Images in (B-C) are a composite of several high-resolution SEM images. Surficial coatings (~100 nm) observed on the side of the left edge of (C) and (D) are silicon redeposition from the FIB polishing processes.
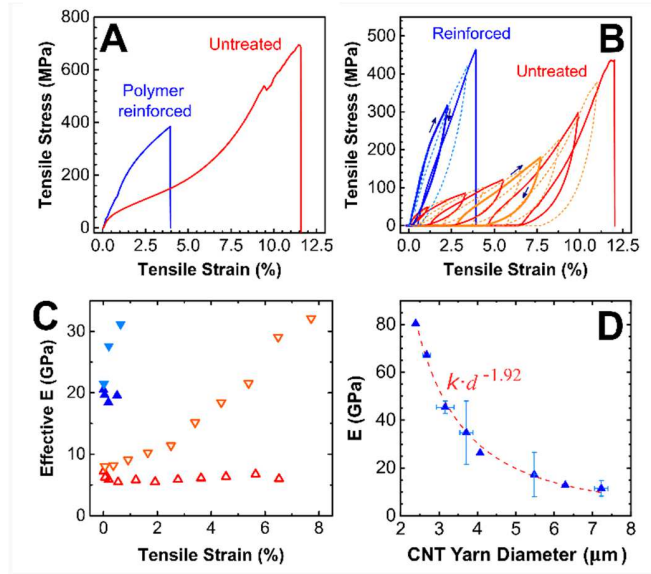
Figure 4. Tensile Properties of Reinforced CNT yarns. (**A**) Stress-strain curves are for identical yarns, ~5.5 μm thick with a twist density of 40,000 turns/m. (**B**) Hysteretic stress-strain curves for dry-spun yarns before and after coating. Cycling was performed by increasing the elongation range by 1% strain at a constant timestep of 70 s for half loading-unloading full-cycle. (**C**) Effective Young's (E_{eff}) modulus computed from the slopes from the beginning of loading (upright triangles) and unloading (downward triangles) curves shown in (B) for each targeted final strain. Blue filled symbols show the E_{eff} values for polymer-reinforced yarns while the red open symbols correspond to untreated yarns. (**D**) Evolution of Young's modulus with diameter for reinforced yarns with twist densities of 40,000 turn/m. Red dashed curve is a power law fitting of E as function of diameter $E \propto d^{-1.92}$, $r^2 = 0.9948$. Each datapoint is the average of individual measurements (N = 2-5) for yarns with diameters within the range (0.5 μm). Error bars in the *x*-axis represent the standard deviation (σ) of individual yarn diameter measurements from the range mean value. Error bars in the *y*-axis are the standard deviation of E measured among independent samples within the range.

Figure 5. Reinforced CNT yarns support spherical boulders in precision assembled components. A single 6 μm diameter CNT yarn spanning across a circular cylindrical opening is strong enough to easily support a 2 mm diameter sphere that is 600 times its mass glued at the yarn's midpoint with minimal deflection.
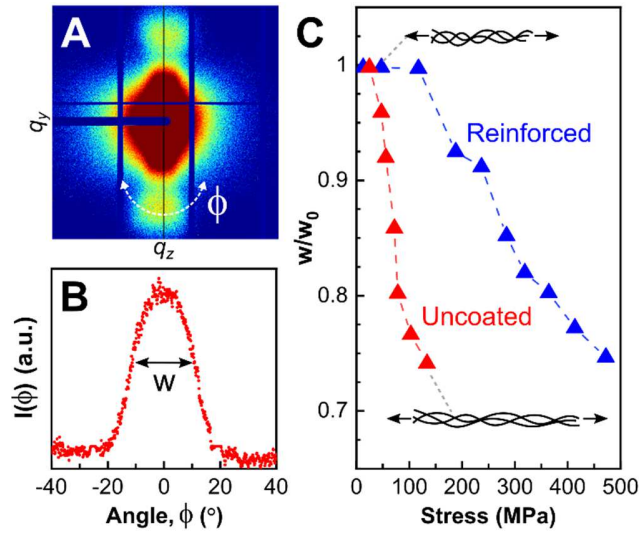
Figure 6. *In-situ* **X-ray scattering of CNT yarns under tensile load.** (**A**) Representative 2D SAXS image collected from an uncoated yarn with mean diameter of 12 µm that was oriented along the q_z direction (spans $\sim \pm 1$ nm^{-1} in both q_y and q_z), where q $= \frac{4\pi}{\lambda}\sin\theta$ and 2θ is the scattering angle. Dashed white lines represent the direction over which intensity was integrated according to the azimuthal angle (ϕ) about the beam direction (into the page). (**B**) Azimuthal intensity distribution I(ϕ) extracted from (A) shows the full-width at half maximum we measured to quantify the distribution width, w, which is indicative of the CNT alignment statistical distribution. (**C**) Relative changes in distribution width as a function of tensile stress, using the initial width prior to loading, w_0, as a reference point. Inset schematics illustrate how the alignment within CNT bundles under tensile loading straighten at low w/w_0 values. Additional experimental details are described in Figure S3, including force versus time, stress versus strain, and w/w_0 at multiple locations along the yarn.
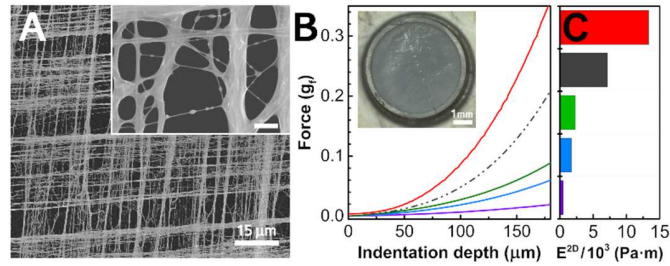
Figure 7. Indentation tests of free-standing CNT sheets. (**A**) Free-standing CNT mesh structure revealed by SEM after IPA aerosol densification and polymer crosslinking. Scalebar in inset is 500 nm. (**B**) Indentation curves of free-standing CNT sheets. Indentation depth is the total distance traveled by the spherical tip-indenter after a first contact with the free-standing CNT mesh. Crosslinked-PGMA reinforced CNT free-standing meshes (red curve) are stronger than free-standing polyimide 40 nm thin films (green) and their reinforced versions with a carbon overcoating (dashed gray line). IPA aerosol densified and untreated free-standing meshes are shown for reference by the blue and purple curves, respectively. Optical image in the *inset* shows the circular film used for indentation experiments after PGMA coating and thermal treatment process (scale bar is 1 mm). (**C**) Two-dimensional elastic moduli (E^{2D}) as extracted from fitting Eq. 3 ($r^2 > 0.9992$ in all cases) to each of the corresponding indentation curves in (A).

Table 1. Fitting parameters obtained from indentation curves for the function $B \cdot x + D \cdot x^3$ and derived values for Young's modulus (E^{2D}) and film pre-tension (σ^{2D}).

Material	B [N/m]	D [Pa/m]	r^2	σ_0^{2D} [N/m]	E^{2D} [Pa·m]
CNT mesh	0.4895	1.793×10^7	0.9992	0.1558	459.4
Densified CNT mesh	1.1648	6.643×10^7	0.9994	0.3708	1702
40 nm PI	1.6923	9.810×10^7	0.9997	0.5387	2305
43 nm PI+C (8 nm)	1.7386	2.979×10^8	0.9999	0.5534	7149
Crosslinked PGMA-CNT mesh	3.2107	5.200×10^8	0.9994	1.022	13324

AUTHOR INFORMATION

Corresponding Author

* Xavier Lepró — Materials Science Department, Lawrence Livermore National Laboratory.
P.O. Box 808, L-474, Livermore, CA 94550, USA. E-mail: xnlepro@llnl.gov

Author Contributions

The manuscript was written through contributions of all authors. All authors have given approval to the final version of the manuscript.

Terry McAfee, Matthew Marcus, and David Kilcoyne regarding X-ray characterization. LLNL-JRNL-818731

REFERENCES

[1] M.-F. Yu, O. Lourie, M.J. Dyer, K. Moloni, T.F. Kelly, R.S. Ruoff, Strength and Breaking Mechanism of Multiwalled Carbon Nanotubes Under Tensile Load, Science 287(5453) (2000) 637-640.

[2] H. Sugime, T. Sato, R. Nakagawa, T. Hayashi, Y. Inoue, S. Noda, Ultra-long carbon nanotube forest via in situ supplements of iron and aluminum vapor sources, Carbon 172 (2021) 772-780.

[3] W. Cho, M. Schulz, V. Shanov, Growth and characterization of vertically aligned centimeter long CNT arrays, Carbon 72 (2014) 264-273.

[4] X. Zhang, W. Lu, G. Zhou, Q. Li, Understanding the Mechanical and Conductive Properties of Carbon Nanotube Fibers for Smart Electronics, Adv. Mater. 32(5) (2020) 1902028.

[5] M. Zhang, K.R. Atkinson, R.H. Baughman, Multifunctional Carbon Nanotube Yarns by Downsizing an Ancient Technology, Science 306(5700) (2004) 1358-1361.

[6] Y.-L. Li, I.A. Kinloch, A.H. Windle, Direct Spinning of Carbon Nanotube Fibers from Chemical Vapor Deposition Synthesis, Science 304(5668) (2004) 276-278.

[7] J. Min, J.Y. Cai, M. Sridhar, C.D. Easton, T. R. Gengenbach, J. McDonnell, W. Humphries, S. Lucas, High performance carbon nanotube spun yarns from a crosslinked network, Carbon 52 (2013) 520-527.

[8] S.-Y. Jeon, J. Jang, B.-W. Koo, Y.-W. Kim, W.-R. Yu, A predictive model of the tensile strength of twisted carbon nanotube yarns, Nanotechnology 28(1) (2016) 015703.

[9] V. Datsyuk, M. Kalyva, K. Papagelis, J. Parthenios, D. Tasis, A. Siokou, I. Kallitsis, C. Galiotis, Chemical oxidation of multiwalled carbon nanotubes, Carbon 46(6) (2008) 833-840.

[10] K. Esumi, M. Ishigami, A. Nakajima, K. Sawada, H. Honda, Chemical treatment of carbon nanotubes, Carbon 34(2) (1996) 279-281.

[11] R. Yu, L. Chen, Q. Liu, J. Lin, K.-L. Tan, S.C. Ng, H.S.O. Chan, G.-Q. Xu, T.S.A. Hor, Platinum Deposition on Carbon Nanotubes via Chemical Modification, Chem. Mater. 10(3) (1998) 718-722.

[12] M.-L. Sham, J.-K. Kim, Surface functionalities of multi-wall carbon nanotubes after UV/Ozone and TETA treatments, Carbon 44(4) (2006) 768-777.

[13] S.C. Wang, K.S. Chang, C.J. Yuan, Enhancement of electrochemical properties of screen-printed carbon electrodes by oxygen plasma treatment, Electrochim. Acta 54(21) (2009) 4937-4943.

[14] Y. Jung, T. Kim, C.R. Park, Effect of polymer infiltration on structure and properties of carbon nanotube yarns, Carbon 88 (2015) 60-69.

[15] B. Vigolo, A. Pénicaud, C. Coulon, C. Sauder, R. Pailler, C. Journet, P. Bernier, P. Poulin, Macroscopic Fibers and Ribbons of Oriented Carbon Nanotubes, Science 290(5495) (2000) 1331-1334.

[16] S. Bal, S.S. Samal, Carbon nanotube reinforced polymer composites—A state of the art, Bull. Mater. Sci. 30(4) (2007) 379.

[17] Q. Cheng, B. Wang, C. Zhang, Z. Liang, Functionalized Carbon-Nanotube Sheet/Bismaleimide Nanocomposites: Mechanical and Electrical Performance Beyond Carbon-Fiber Composites, Small 6(6) (2010) 763-767.

[18] J.Y. Cai, J. Min, J. McDonnell, J.S. Church, C.D. Easton, W. Humphries, S. Lucas, A.L. Woodhead, An improved method for functionalisation of carbon nanotube spun yarns with aryldiazonium compounds, Carbon 50(12) (2012) 4655-4662.

[19] O.-K. Park, W. Lee, J.Y. Hwang, N.-H. You, Y. Jeong, S.M. Kim, B.-C. Ku, Mechanical and electrical properties of thermochemically cross-linked polymer carbon nanotube fibers, Compos. Part A Appl. 91 (2016) 222-228.

[20] O.-K. Park, H. Choi, H. Jeong, Y. Jung, J. Yu, J.K. Lee, J.Y. Hwang, S.M. Kim, Y. Jeong, C.R. Park, M. Endo, B.-C. Ku, High-modulus and strength carbon nanotube fibers using molecular cross-linking, Carbon 118 (2017) 413-421.

[21] F. Meng, X. Zhang, R. Li, J. Zhao, X. Xuan, X. Wang, J. Zou, Q. Li, Electro-Induced Mechanical and Thermal Responses of Carbon Nanotube Fibers, Adv. Mater. 26(16) (2014) 2480-2485.

[22] Z. Spitalsky, D. Tasis, K. Papagelis, C. Galiotis, Carbon nanotube–polymer composites: Chemistry, processing, mechanical and electrical properties, Prog. Polym. Sci. 35(3) (2010) 357-401.

[23] C.A.C. Chazot, C.K. Jons, A.J. Hart, In Situ Interfacial Polymerization: A Technique for Rapid Formation of Highly Loaded Carbon Nanotube-Polymer Composites, Adv. Funct. Mater. 30(52) (2020) 2005499.

[24] A. Kis, G. Csányi, J.P. Salvetat, T.-N. Lee, E. Couteau, A.J. Kulik, W. Benoit, J. Brugger, L. Forró, Reinforcement of single-walled carbon nanotube bundles by intertube bridging, Nat. Mater. 3(3) (2004) 153-157.

[25] J. Di, S. Fang, F.A. Moura, D.S. Galvão, J. Bykova, A. Aliev, M.J. de Andrade, X. Lepró, N. Li, C. Haines, R. Ovalle-Robles, D. Qian, R.H. Baughman, Strong, Twist-Stable Carbon Nanotube Yarns and Muscles by Tension Annealing at Extreme Temperatures, Adv. Mater. 28(31) (2016) 6598-6605.

[26] S.H. Baxamusa, K.K. Gleason, Thin Polymer Films with High Step Coverage in Microtrenches by Initiated CVD, Chem. Vap. Depos. 14(9-10) (2008) 313-318.

[27] M. Gupta, V. Kapur, N.M. Pinkerton, K.K. Gleason, Initiated Chemical Vapor Deposition (iCVD) of Conformal Polymeric Nanocoatings for the Surface Modification of High-Aspect-Ratio Pores, Chem. Mater. 20(4) (2008) 1646-1651.

[28] A. Asatekin, K.K. Gleason, Polymeric Nanopore Membranes for Hydrophobicity-Based Separations by Conformal Initiated Chemical Vapor Deposition, Nano Lett. 11(2) (2011) 677-686.

[29] V. Thiagarajan, X. Wang, P.D. Bradford, Y.T. Zhu, F.G. Yuan, Stabilizing carbon nanotube yarns using chemical vapor infiltration, Compos Sci Technol 90 (2014) 82-87.

[30] J. Lee, T. Kim, Y. Jung, K. Jung, J. Park, D.-M. Lee, H.S. Jeong, J.Y. Hwang, C.R. Park, K.-H. Lee, S.M. Kim, High-strength carbon nanotube/carbon composite fibers via chemical vapor infiltration, Nanoscale 8(45) (2016) 18972-18979.

[31] K.K.S. Lau, K.K. Gleason, Initiated Chemical Vapor Deposition (iCVD) of Poly(alkyl acrylates): A Kinetic Model, Macromolecules 39(10) (2006) 3695-3703.

[32] Y. Ye, Y. Mao, F. Wang, H. Lu, L. Qu, L. Dai, Solvent-free functionalization and transfer of aligned carbon nanotubes with vapor-deposited polymer nanocoatings, J. Mater. Chem. 21(3) (2011) 837-842.

[33] H. Sojoudi, S. Kim, H. Zhao, R.K. Annavarapu, D. Mariappan, A.J. Hart, G.H. McKinley, K.K. Gleason, Stable Wettability Control of Nanoporous Microstructures by iCVD Coating of Carbon Nanotubes, ACS Appl. Mater. Interfaces 9(49) (2017) 43287-43299.

[34] K.K. Gleason, Overview of Chemically Vapor Deposited (CVD) Polymers, CVD Polymers 2015, pp. 1-11.

[35] X. Lepró, P. Ehrmann, J. Menapace, J. Lotscher, S. Shin, R. Meissner, S. Baxamusa, Ultralow stress, thermally stable cross-linked polymer films of polydivinylbenzene (PDVB), Langmuir 33(21) (2017) 5204-5212.

[36] X. Lepró, R. Ovalle-Robles, M.D. Lima, A.L. Elías, M. Terrones, R.H. Baughman, Catalytic Twist-Spun Yarns of Nitrogen-Doped Carbon Nanotubes, Adv. Funct. Mater. 22(5) (2012) 1069-1075.

[37] E.A. Ali, H.L. Marcio, M.S. Edward, H.B. Ray, Thermal conductivity of multi-walled carbon nanotube sheets: radiation losses and quenching of phonon modes, Nanotechnology 21(3) (2010) 035709.

[38] J.F. Shackelford, W. Alexander, CRC Materials Science and Engineering Handbook, Taylor & Francis, 2000, p. 1980.

[39] A. Suresh, D. Anastasio, D.D. Burkey, Potential of Hexyl Acrylate Monomer as an Initiator in Photo-initiated CVD, Chem. Vap. Depos. 20(1-2-3) (2014) 5-7.

[40] G. Ozaydin-Ince, K.K. Gleason, Tunable Conformality of Polymer Coatings on High Aspect Ratio Features, Chem. Vap. Depos. 16(1-3) (2010) 100-105.

[41] V.J.B. Jeevendrakumar, D.N. Pascual, M. Bergkvist, Wafer Scale Solventless Adhesive Bonding with iCVD Polyglycidylmethacrylate: Effects of Bonding Parameters on Adhesion Energies, Adv. Mater. Interfaces 2(9) (2015) 1500076.

[42] S.O. Kucheyev, M. Stadermann, S.J. Shin, J.H. Satcher, S.A. Gammon, S.A. Letts, T. van Buuren, A.V. Hamza, Super-Compressibility of Ultralow-Density Nanoporous Silica, Adv. Mater. 24(6) (2012) 776-780.

[43] F. Espinosa-Loza, M. Stadermann, C. Aracne-Ruddle, R. Casey, P. Miller, R. Whitesides, Modeling the mechanical properties of ultra-thin polymer films, High Power Laser Sci. Eng. 5 (2017) e27.

[44] T. Warwick, H. Ade, D. Kilcoyne, M. Kritscher, T. Tylisczcak, S. Fakra, A. Hitchcock, P. Hitchcock, H. Padmore, A new bend-magnet beamline for scanning transmission X-ray microscopy at the Advanced Light Source, J. Synchrotron Radiat. 9(4) (2002) 254-257.

[45] A. Hexemer, W. Bras, J. Glossinger, E. Schaible, E. Gann, R. Kirian, A. MacDowell, M. Church, B. Rude, H. Padmore, A SAXS/WAXS/GISAXS Beamline with Multilayer Monochromator, J. Phys. Conf. Ser. 247 (2010) 012007.

[46] K. Sears, C. Skourtis, K. Atkinson, N. Finn, W. Humphries, Focused ion beam milling of carbon nanotube yarns to study the relationship between structure and strength, Carbon 48(15) (2010) 4450-4456.

[47] Y. Mao, K.K. Gleason, Hot Filament Chemical Vapor Deposition of Poly(glycidyl methacrylate) Thin Films Using tert-Butyl Peroxide as an Initiator, Langmuir 20(6) (2004) 2484-2488.

[48] Q. Lu, G. Keskar, R. Ciocan, R. Rao, R.B. Mathur, A.M. Rao, L.L. Larcom, Determination of Carbon Nanotube Density by Gradient Sedimentation, J. Phys. Chem. B 110(48) (2006) 24371-24376.

[49] M. Miao, J. McDonnell, L. Vuckovic, S.C. Hawkins, Poisson's ratio and porosity of carbon nanotube dry-spun yarns, Carbon 48(10) (2010) 2802-2811.

[50] K. Liu, Y. Sun, R. Zhou, H. Zhu, J. Wang, L. Liu, S. Fan, K. Jiang, Carbon nanotube yarns with high tensile strength made by a twisting and shrinking method, Nanotechnology 21(4) (2009) 045708.

[51] J.-W. Kim, G. Sauti, R.A. Wincheski, R.J. Cano, B.D. Jensen, J.G. Smith Jr., K.E. Wise, E.J. Siochi, Undirectional Carbon Nanotube Yarn/Polymer Composites, NASA, Langley Research Center. Hampton, Virginia 23681-2199, 2018, p. 37.

[52] P.D. Bradford, A.E. Bogdanovich, Carbon nanotube yarn and 3-D braid composites. Part II: Dynamic mechanical analysis, Compos. Part A Appl. 41(2) (2010) 238-246.

[53] M. Zhang, S. Fang, A.A. Zakhidov, S.B. Lee, A.E. Aliev, C.D. Williams, K.R. Atkinson, R.H. Baughman, Strong, Transparent, Multifunctional, Carbon Nanotube Sheets, Science 309(5738) (2005) 1215-1219.

[54] C. Lee, X. Wei, J.W. Kysar, J. Hone, Measurement of the Elastic Properties and Intrinsic Strength of Monolayer Graphene, Science 321(5887) (2008) 385-388.

[55] Z. Huo, Z. Guo, J. Leng, T. Chang, Nanoindentation of circular multilayer graphene allotropes, Sci. China Technol. Sci. 62(2) (2019) 269-275.

[56] L. Chen, C. Liu, J. Wang, W. Zhang, C. Hu, S. Fan, Auxetic materials with large negative Poisson's ratios based on highly oriented carbon nanotube structures, Applied Physics Letters 94(25) (2009) 253111.

[57] O.L. Blakslee, D.G. Proctor, E.J. Seldin, G.B. Spence, T. Weng, Elastic Constants of Compression-Annealed Pyrolytic Graphite, J. Appl. Phys. 41(8) (1970) 3373-3382.

[58] C.L. Bauer, R.J. Farris, Determination of poisson's ratio for polyimide films, Polym. Eng. Sci. 29(16) (1989) 1107-1110.

① Draw a CNT sheet

Twist into a yarn

Stack free-standing sheets

iCVD

② PGMA coating

③ PGMA crosslinking

150-180°C

2.1 Aerosol densification

IPA

2.2 Sheet collapses in z

6 μm yarn

600x mass

1 mm